



Characterization of the DART Impact Ejecta Plume on Dimorphos from LICIAcube Observations

J. D. P. Deshapriya¹ , P. H. Hasselmann¹ , I. Gai², M. Hirabayashi³ , E. Dotto¹, A. Rossi⁴ , A. Zinzi⁵ , V. Della Corte⁶, I. Bertini^{7,8}, S. Ieva¹ , E. Mazzotta Epifani¹, M. Dall'Ora⁹ , S. Ivanovski¹⁰ , D. Perna¹ , T. L. Farnham¹¹ , M. Amoroso⁵, J. R. Brucato¹² , A. Capannolo¹³, S. Caporali¹², M. Ceresoli¹³, Nancy L. Chabot¹⁴ , A. Cheng¹⁴, G. Cremonese¹⁵ , R. T. Daly¹⁴ , E. G. Fahnestock¹⁶, L. Gomez Casajus², E. Gramigna², G. Impresario⁵, R. Lasagni Manghi², M. Lavagna¹³, J.-Y. Li¹⁷, M. Lombardo², A. Lucchetti¹⁵, D. Modenini⁹, M. Pajola¹⁵ , E. Palmer¹⁷ , P. Palumbo^{7,8} , S. Pirrotta⁵, G. Poggiali^{12,18} , A. S. Rivkin¹⁴ , P. Sanchez¹⁹ , G. Tancredi²⁰ , P. Tortora², F. Tusberti¹⁵, M. Zannoni², and G. Zanotti¹³

¹ INAF-Osservatorio Astronomico di Roma Via Frascati 33, I-00078 Monte Porzio Catone (Rome), Italy; prasanna.deshapriya@inaf.it

² Università di Bologna, Bologna, Italy

³ Daniel Guggenheim School of Aerospace Engineering, Georgia Institute of Technology 620 Cherry Street, Atlanta GA 30332, USA

⁴ CNR Istituto di Fisica Applicata "Nello Carrara," Sesto Fiorentino (Firenze), Italy

⁵ Agenzia Spaziale Italiana, Roma, Italy

⁶ IAPS-INAf, Roma, Italy

⁷ Università degli Studi di Napoli "Parthenope," Napoli, Italy

⁸ INAF Istituto di Astrofisica e Planetologia Spaziali, Roma, Italy

⁹ INAF Osservatorio Astronomico di Capodimonte, Napoli, Italy

¹⁰ INAF Osservatorio Astronomico di Trieste, Italy

¹¹ University of Maryland, Department of Astronomy, MD, USA

¹² INAF Osservatorio Astrofisico di Arcetri, Firenze, Italy

¹³ Politecnico di Milano, Italy

¹⁴ Johns Hopkins University Applied Physics Laboratory, Laurel, MD, USA

¹⁵ INAF Osservatorio Astronomico di Padova, Italy

¹⁶ Jet Propulsion Laboratory, California Institute of Technology 4800 Oak Grove Drive, Pasadena, CA 91109, USA

¹⁷ Planetary Science Institute, Tucson, AZ, USA

¹⁸ Observatoire de Paris, France

¹⁹ Colorado Center for Astrodynamics Research, University of Colorado Boulder 3775 Discovery Drive, Boulder, CO 80303, USA

²⁰ Departamento de Astronomía, Facultad de Ciencias, Iguá 4225, 11400 Montevideo, Uruguay

Received 2023 September 27; revised 2023 November 2; accepted 2023 November 2; published 2023 December 7

Abstract

We modeled the geometry and the three-dimensional orientation of the ejecta cone triggered by the impact of the DART spacecraft on the asteroid Dimorphos. We used eight LUKE images of the impact acquired by the CubeSat LICIAcube that flew by the Didymos system shortly after the impact. These images, which show the ejecta cone in both face-on and side-on profiles, enabled us to reconstruct the ejecta cone in inertial space. We started our model as a simple cone with a circular base and developed it to a rotated cone with an elliptical base that best fit the data. The cone axis points to R.A., decl. (in J2000): 147_{-10}^{+1} °, $+16_{-6}^{+4}$ °. The cone is characterized by two perpendicular half-angles of $\eta = 69_{-3}^{+1}$ °, $\gamma = 51_{-11}^{+1}$ ° and a rotation of $\omega = 12$ ° around its axis. The apex of the cone is located near the center of Dimorphos within 15 m. The intersection of the cone and the surface of Dimorphos (surface enclosed by the cone) would correspond to a crater with a maximum radius of about 65 m. The characterization of the cone axis is directly related to the computation of the momentum enhancement factor (β) of the impact, and it hence proves the crucial need of studying impacts in the context of planetary defence scenarios. The results of this work could potentially be used to constrain whether the impact took place in a strength-dominated or a gravity-dominated regime. This work shows the important scientific return of the LICIAcube CubeSat in the context of planetary defence.

Unified Astronomy Thesaurus concepts: [Asteroids \(72\)](#)

1. Introduction

The NASA Double Asteroid Redirection Test (DART) mission performed a kinetic impact on asteroid Dimorphos, the satellite of the binary asteroid (65803) Didymos, at 23:14 UTC on 2022 September 26 as a planetary defence test (Cheng et al. 2018). DART was the first hypervelocity impact experiment on an asteroid at size and velocity scales relevant to planetary defence, intended to validate kinetic impact as a means of

asteroid deflection. The ensuing momentum transfer reduced the orbital period of Dimorphos by 33.0 ± 1.0 (3σ) minutes (Thomas et al. 2023), successfully achieving the goal of the DART mission. The determination of the momentum transferred to Dimorphos by the DART impact can be characterized by the momentum enhancement factor, β , which was estimated to be in the range between 2.2 and 4.9 (Cheng et al. 2023), depending on the mass of Dimorphos (if the Dimorphos bulk density were in the range of 1500 to 3300 kg m^{-3}). These values imply that the amount of momentum transferred due to the recoil force received from escaping ejecta material was significantly larger than the entire momentum transferred by the impacting DART spacecraft alone in a perfectly inelastic

collision. In this latter case, β would have been one (Cheng et al. 2018), and the reduction of the orbital period would have been about 7 minutes (Rivkin et al. 2021). This agrees with the impact simulation scenarios performed prior to the DART impact with different combinations of potential impact conditions and asteroid physical properties (Raducan & Jutzi 2022; Stickle et al. 2022). If the impactor were to generate an ejecta curtain, the determination of β becomes dependent on the characterization of the ejecta plume, which is usually modeled as a cone. In the context of the DART mission, it was therefore necessary to determine the direction of the net ejecta momentum in inertial space. This is where the data returned by the Italian Space Agency's 6U CubeSat LICIAcube become important because it flew by the Didymos system and acquired images both prior to and after the DART impact from varying vantage points (Dotto et al. 2021). LICIAcube was initially housed inside the DART spacecraft and was released 15 days prior to the impact. After performing two orbital manoeuvres, the satellite was able to witness the impact and its aftermath at varying spatial resolutions and phase angles, thanks to its two imaging cameras LEIA and LUKE. The aftermath of the impact was also observed using Hubble Space Telescope data by Li et al. (2023) complimentary to LICIAcube data, and this enabled the characterization of the evolving ejecta. Recently, Hirabayashi et al. (2023) applied Hubble Space Telescope (HST) and LUKE images to determine the cone geometry by introducing the assumption that the cone geometry is elliptical. They found that the cone is indeed elliptical. In this work, we use a different approach and start to model the cone with a simple cone with a circular base and show why it does not fit the data, and we explain the need to use a cone with an elliptical base including rotation to fit the data better. We show that the geometric problem of the ejecta cone can be solved with LICIAcube LUKE images alone, and as discussed below, our solutions are consistent with those reported in Hirabayashi et al. (2023).

2. Methods and Results

2.1. A Cone with a Circular Base

We first assume that the ejecta plume can be approximated by a cone with a circular base. Under this assumption, we use the relation of a cone and its projection onto a plane, as illustrated in Figure 1 and parameterized in Equation (1), because we worked with LUKE data, for which the images were acquired in the LUKE image plane. With respect to Figure 1, α is the half aperture angle of the original cone, δ is the half aperture angle of the projected cone, and θ is the angle between the cone axis and the image plane,

$$\tan(\delta) = \frac{\tan(\alpha)}{\sqrt{\cos^2(\theta) - \tan^2(\alpha)\sin^2(\theta)}}. \quad (1)$$

We have a sequence of five LUKE images, where the ejecta cone can be seen in a side-on profile (Figure 2), allowing us to measure 2δ when the cone edges are defined. These measurements are reported in Table 1 with their uncertainties, which are associated with the definition of the cone edges themselves. The context of the flyby and the instances where the images have been acquired are visualized in Figure 3. We rearrange Equation (1) to obtain Equation (2), which isolates α , which is

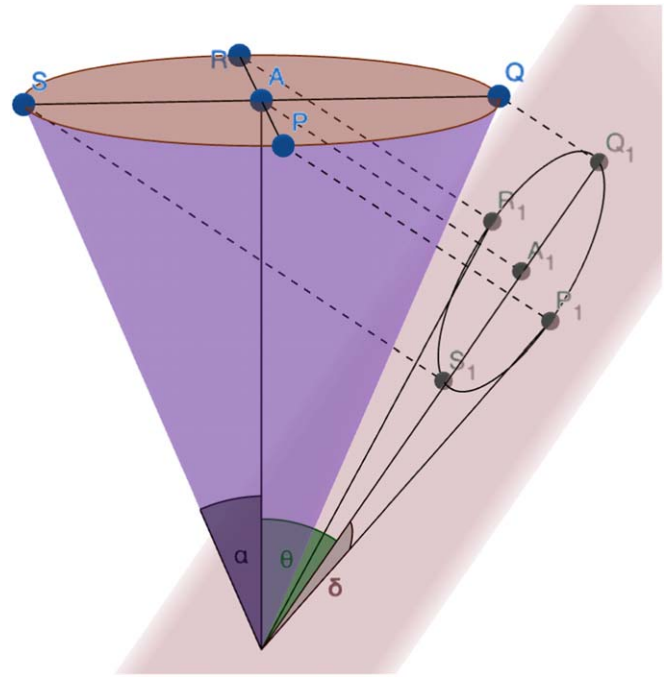


Figure 1. A cone with a circular base and its projection onto a plane.

one of the variables for which we have to solve,

$$\tan(\alpha) = \frac{\tan(\delta)\cos(\theta)}{\sqrt{1 + \tan^2(\delta)\sin^2(\theta)}}. \quad (2)$$

Currently, α and θ remain unknown. However, we do have indirect information about θ because we can recover the image plane for each LUKE observation in inertial space using the SPICE kernels (Acton 1996; Acton et al. 2018) of LICIAcube. Therefore, we are able to recover the coefficients that define the plane, allowing us to formulate $a_n x + b_n y + c_n z + d_n = 0$ as the plane for each observation in an inertial coordinate system of the x , y , and z axes. The subscript n of the coefficient defines the observation ID. Next, we define the axis of the ejecta cone as $px + qy + rz$ in inertial space and assume it to be a unit vector. The p , q , and r coefficients need to be solved for. The formulations of the equation of the plane and the aforementioned unit vector equation allow us to replace θ in Equation (2) by the coefficients defined above. By rearranging Equation (2), we formulate a nonlinear equation for each of the observations, as can be seen from Equation (3) through Equation (7), where abc_{ij} corresponds to the i th observation, and j refers to the coefficient of the x , y , or z component of the corresponding equation of the plane. We are therefore left with four unknowns, p , q , r , and $\tan(\alpha)$, for which we need to solve,

$$f_1 = -\tan^2(\alpha) + \tan^2(\delta)_1 \left(1 - \frac{(abc_{10}(p) + abc_{11}(q) + abc_{12}(r))^2}{(abc_{10}^2 + abc_{11}^2 + abc_{12}^2)} (1 + \tan^2(\alpha)) \right) = 0 \quad (3)$$

$$f_2 = -\tan^2(\alpha) + \tan^2(\delta)_2 \left(1 - \frac{(abc_{20}(p) + abc_{21}(q) + abc_{22}(r))^2}{(abc_{20}^2 + abc_{21}^2 + abc_{22}^2)} (1 + \tan^2(\alpha)) \right) = 0 \quad (4)$$

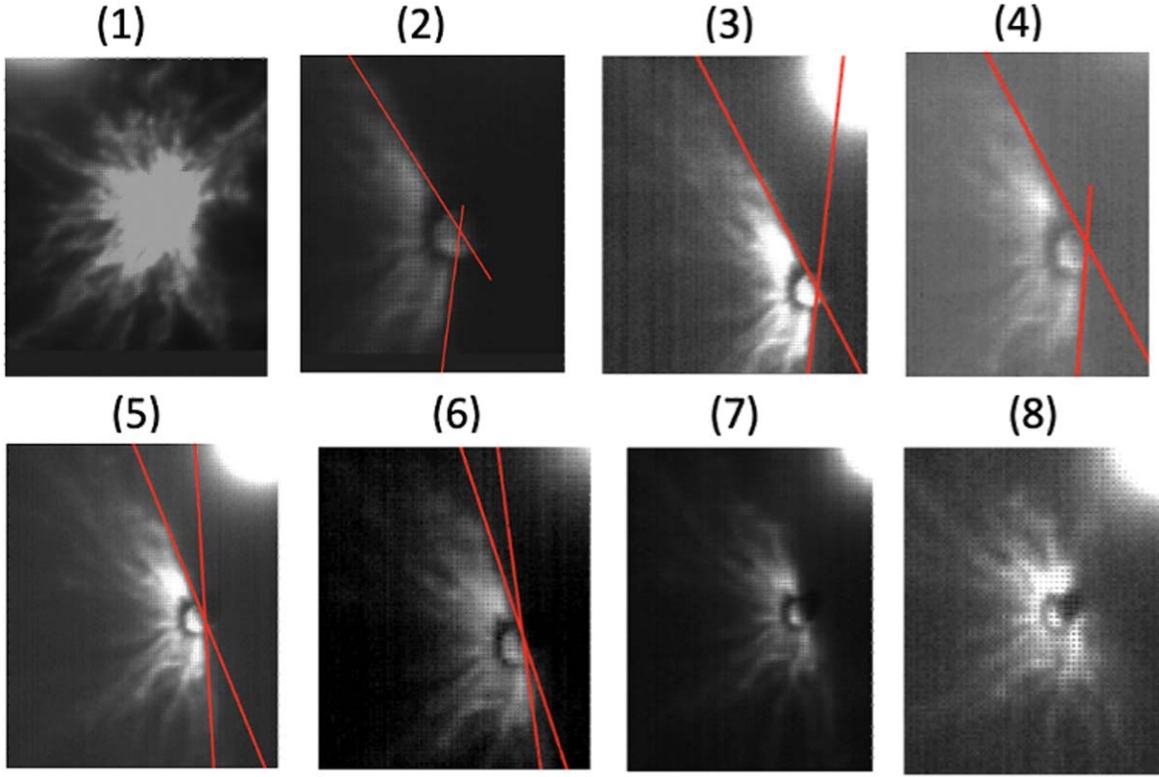


Figure 2. A sequence of LUKE images where the ejecta cone can be seen in a face-on profile (ID 1), in a side-on profile (IDs 2 to 6), and transitioning from a side-on profile to a view from behind (IDs 7 and 8). The images have been cropped to highlight the ejecta cone. The red lines in IDs 2 to 6 guide the eye through the edges of the projected cone. The edges serve for the measurement of the aperture angle of the projected cone 2δ . These angular measurements and some information about the images are given in Table 1. Except for ID 1, Dimorphos can be seen in other images with a shadow cast by the optically thick part of the ejecta cone. The very bright object in the corner of some of the images is Didymos, which is inside the crop.

$$f_3 = -\tan^2(\alpha) + \tan^2(\delta) \left(1 - \frac{(abc_{30}(p) + abc_{31}(q) + abc_{32}(r))^2}{(abc_{30}^2 + abc_{31}^2 + abc_{32}^2)} (1 + \tan^2(\alpha)) \right) = 0 \quad (5)$$

$$f_4 = -\tan^2(\alpha) + \tan^2(\delta) \left(1 - \frac{(abc_{40}(p) + abc_{41}(q) + abc_{42}(r))^2}{(abc_{40}^2 + abc_{41}^2 + abc_{42}^2)} (1 + \tan^2(\alpha)) \right) = 0 \quad (6)$$

$$f_5 = -\tan^2(\alpha) + \tan^2(\delta) \left(1 - \frac{(abc_{50}(p) + abc_{51}(q) + abc_{52}(r))^2}{(abc_{50}^2 + abc_{51}^2 + abc_{52}^2)} (1 + \tan^2(\alpha)) \right) = 0 \quad (7)$$

$$f_6 = p^2 + q^2 + r^2 - 1 = 0. \quad (8)$$

However, we have five equations for the five observations and the unit vector equation, which means six equations in total. Because we need to solve for four unknowns, there are 15 unique ways in which we can form a system of four simultaneous nonlinear equations. We systematically proceed to solve each system of nonlinear equations numerically, using the Python library `scipy (optimize.roots)`, which takes an initial guess for the coefficients p , q , r , and the half aperture angle α (Chen & Stadherr 1981). This routine returns a solution and a flag whether the solution converges or not, and we only proceed with the solutions that do converge. It should be highlighted that this method does not give a unique solution because there are multiple ways of forming the system of

nonlinear equations that are to be solved. Therefore, for each obtained converged axis solution, we rotate the solved axis such that its projection lies within a degree from the bisector of the projected cone aperture angle in the LUKE images (this bisector is also assumed as the axis of the ejecta cone). The rotated solutions visualized in the LUKE frame are then compared against real LUKE images for consistency and are rejected if they do not match. For this comparison, we use the LUKE observations (IDs 1 to 6). Inclusion of the image ID 1 is crucial in this step, as it brings independent verification of the solutions due to its very different vantage point compared to IDs 2 to 6, which go as inputs to the solving routine. The best-fit solution returned by this solving routine is a cone with an aperture angle of 122° , with its axis pointing to right ascension and declination (R.A., decl.): $136^\circ, +5^\circ$ in the J2000 reference frame (Acton 1996; Acton et al. 2018). This solution is obtained by solving the system of equations formed by Equations (4), (6), (7), and (8). Figure 4 illustrates the simulations of the ejecta cone with this solution for the same timestamps as for observation IDs 1-6 as seen from the LUKE frame.

The comparison of the real LUKE images (Figure 2) and the simulated solutions (Figure 4) indicates that although the simulated cone axis seems to be pointing in the correct direction, the aperture angle of the solution does not reproduce all analyzed LUKE observations accurately. For this reason, we begin to model the cone as a cone with an elliptical base.

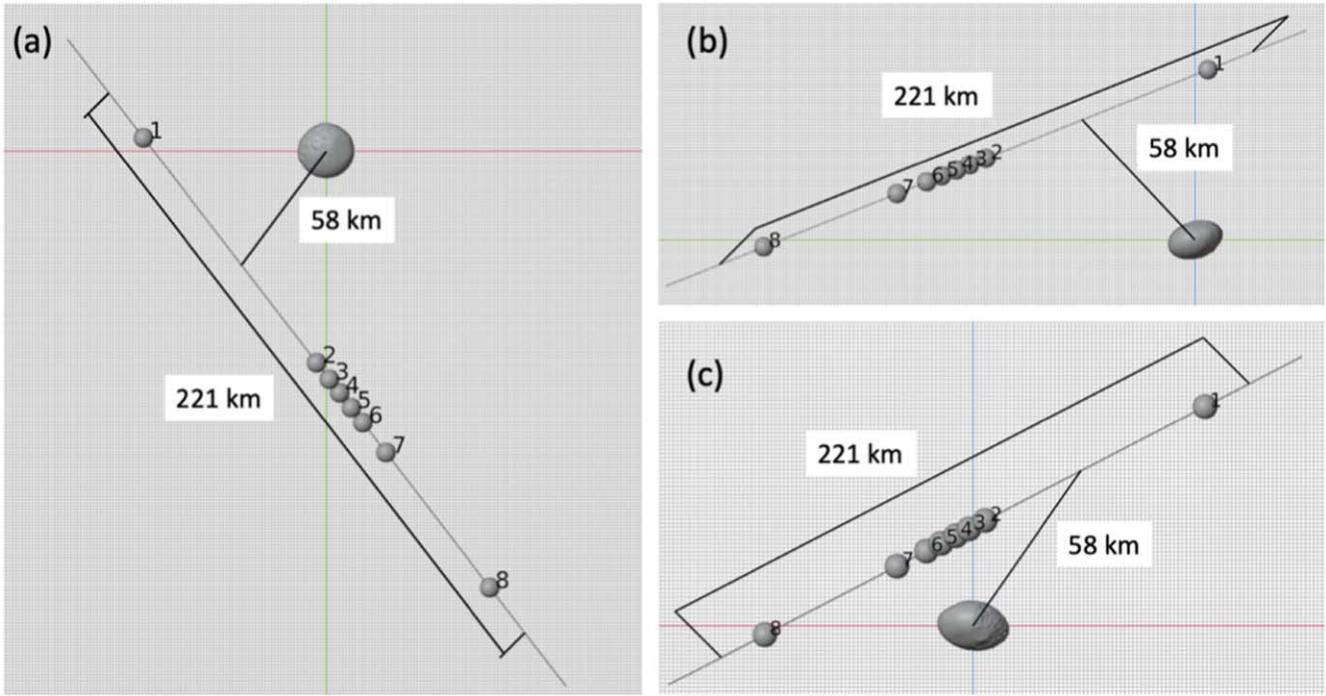


Figure 3. Context of the images from the LICIACube flyby of the Didymos system that are part of this analysis. The diagonal line is the trajectory of the LICIACube CubeSat as it flew by the Didymos system, and the exaggerated dots along this trajectory mark the instances of images 1 to 8, referred to in the Figure 2 and Table 1. Dimorphos is placed at the center of the J2000 coordinate system and is scaled up by a factor of 100 to improve its visibility. Panels (a), (b), and (c) show three orthogonal views of the flyby context in the XY, YZ, and XZ planes in J2000. The closest approach of LICIACube to Dimorphos took place at a distance of about 58 km, and this instance is given as a reference. The blue, red, and green axes correspond to the X, Y, and Z axes, respectively, in J2000.

Table 1
Ancillary Information About LUKE Images That Were Used for the Analysis of the Ejecta Cone (Figure 2)

Image ID	Timestamp (UTC)	Exposure Time (ms)	Time Since Impact (s)	Measured Projected Cone Aperture Angle 2δ ($^{\circ} \pm 2^{\circ}$)
1	2022-09-26T23:17:03.004	4	159	...
2	2022-09-26T23:17:18.000	0.5	174	140
3	2022-09-26T23:17:19.100	0.3	175	145
4	2022-09-26T23:17:20.000	0.2	176	147
5	2022-09-26T23:17:21.000	0.7	177	160
6	2022-09-26T23:17:22.000	0.3	178	170
7	2022-09-26T23:17:24.000	0.7	180	180
8	2022-09-26T23:17:33.000	0.5	189	...

Note. Timestamp indicates the image acquisition time.

2.2. A Cone with an Elliptical Base

We use a model of the cone with an elliptical base, as illustrated in Figure 5. By systematically varying the values of the half-angles η and γ and by using a small enough angular step, we can sample all the cones with an elliptical base that could exist. Each cone is described by 32 vertices populated along the base of the cone, and by one vertex located at its apex. The base of the cone is an ellipse whenever $\eta \neq \gamma$. We then orient the cones along our solved axis and simulate how they would appear in the LUKE frame at different times of observations. Given the prior knowledge about the geometrical nature of ejecta cone, we restrict the possible angular space of both η and γ to be between 10° and 88° . We thus sample all possible cones in this angular space with a step of 1° .

Then, we attempt to compute the projected aperture angle (2δ) of a given cone with an elliptical base projected onto the LUKE plane. To achieve this, we project each vertex onto the LUKE frame and compute the angular separation of each vertex from the axis of the cone projected onto the LUKE frame. While doing this, we track whether the projection of the vertex lies above or below the projected cone axis by using their cross product. Hence, we can find the two most extreme vertices that define the edges of the angle 2δ . The sum of their angular separation from the projected cone axis gives the value of 2δ . We are then able to compare the simulated values of 2δ against the values of 2δ that were measured on real LUKE images and are reported in Table 1 (IDs 2 to 6). Therefore, for each simulation of a cone described by a given permutation of η and γ , we can give a score that tells how good or poor it fits the LUKE observations. The score is defined as the absolute

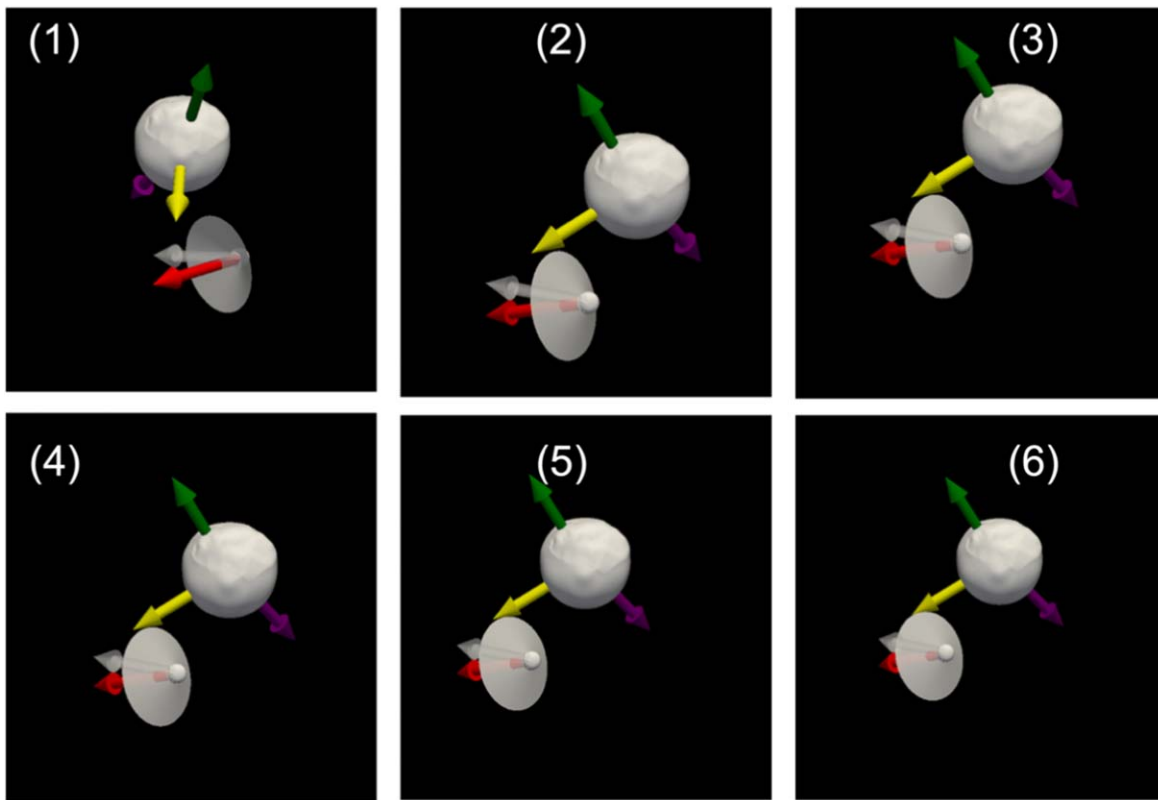


Figure 4. Simulations of the ejecta cone using a cone with a circular base corresponding to LUKE observation IDs 1-6. The cone has an aperture angle of 122° , and its axis points to R.A., decl.: $136^\circ, +5^\circ$ in J2000. Several vectors are shown for reference: Red is the cone axis, gray is the incoming direction of the DART spacecraft, green is the north celestial pole, purple is the north pole of Didymos, and yellow is the direction of the Sun. Illumination effects and shadowing are not considered in this figure.

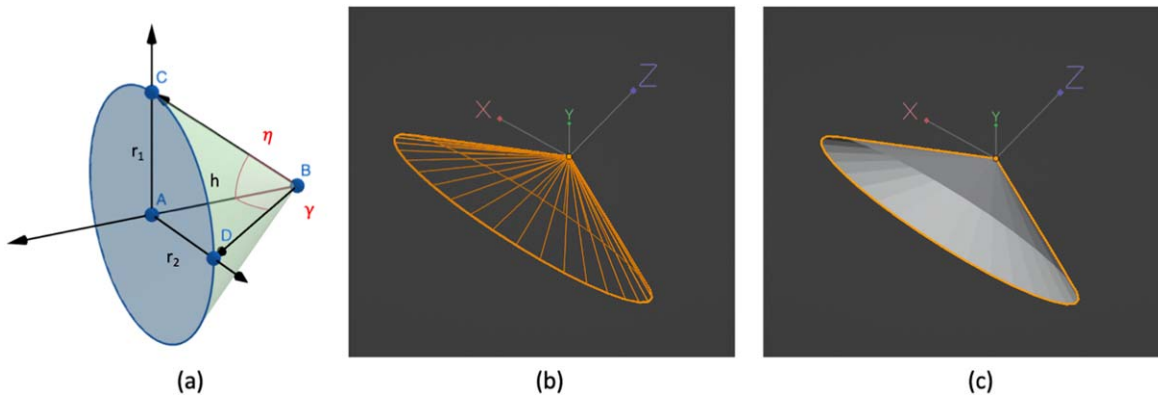


Figure 5. (a) Model of a cone with an elliptical base, described by two orthogonal half-angles η and γ , defined in the BAC plane and BAD plane, respectively. The cone axis points in the BA direction. (b) An example case of such a cone with $\eta = 60^\circ$ and $\gamma = 30^\circ$, described by 33 vertices. The local Cartesian coordinate system is also defined, with the origin being at the apex. (c) The same cone with its cross section highlighted. Note that the cone axis points in the negative Z direction of the local cone coordinate system.

difference between the simulated 2δ and the measured 2δ . For a given cone, we compute a score for each LUKE observation in this way, corresponding to IDs 2 to 7 and the sum of the scores recorded. After we iterate over the restricted space of η and γ , we have a total score for each cone. The minimum total scores would then correspond to the best candidate cones that describe the LUKE observations.

To make these iterations more efficient, we applied another constraint to the orientation of the projected cone such that if a

given cone does not fit an observation ID within a given uncertainty, it will not be iterated for the subsequent observations IDs, and hence will be discarded by assigning a very high score. This constraint was placed by comparing the angular separation between the lowest vertex of a simulated and projected cone and the vertical axis of the LUKE frame. The uncertainty was assigned to be $\pm 4^\circ$ owing to the difficulties associated with defining the ejecta cone edges in LUKE images. The projections must therefore lie $\pm 4^\circ$ from the

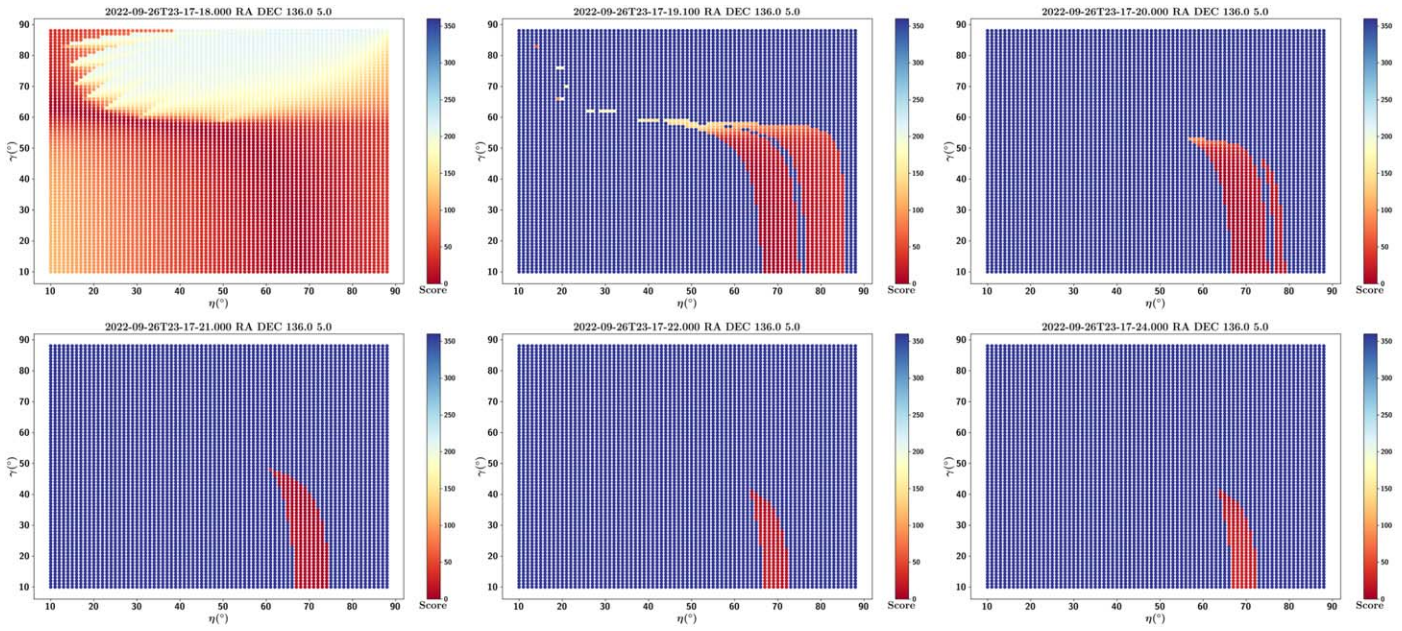


Figure 6. Each panel corresponds to a LUKÉ observation where the ejecta cone is observed projected in a side-on profile or a similar geometry. The corresponding timestamps are given in the panel titles. The first panel explores all cones with an elliptical base in the selected restricted η and γ space, and their scores are given in the scatter plot. The following panels show how the scores evolve for a given cone, as constraints are placed by different LUKÉ observations. The panels should be followed from left to right and top to bottom. Thus, the last panel isolates the viable solutions of η and γ that best describe the LUKÉ observations. The contrasting very high scores correspond to η and γ combinations that are discontinued from the iterations as they do not fall within the imposed cone edge orientation constraints.

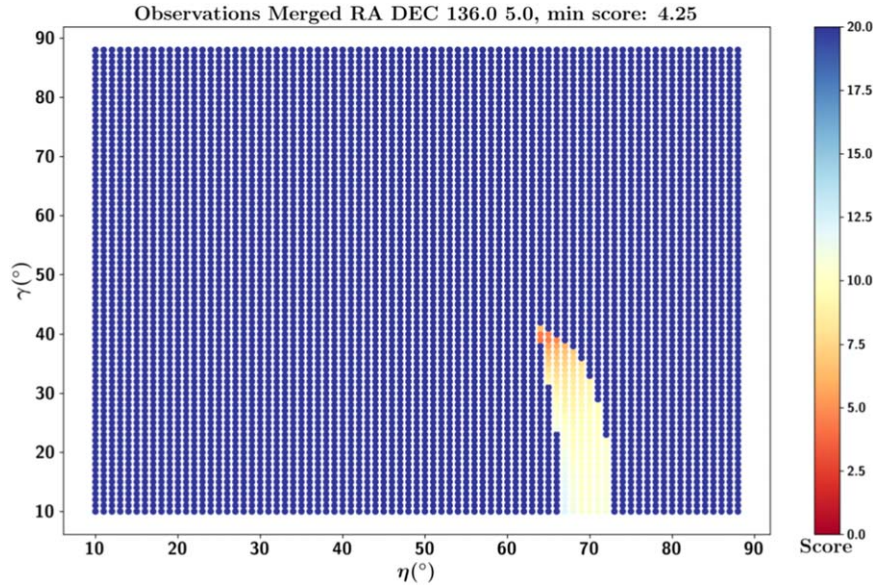


Figure 7. The scores shown in different panels of Figure 6 are averaged here and are represented in a narrower scale than in Figure 6 in order to highlight the viable solutions of η and γ .

lowest edge of the projected cone in real LUKÉ images. This iterative process is illustrated in Figure 6, and the outcome of this constraint placement is given in Figure 7.

As can be seen in Figure 7, the minimum average score is 4.25 , and it corresponds to $\eta = 64^\circ$, $\gamma = 39^\circ$. However, due to the aforementioned uncertainties, we allow a tolerance when accepting viable solutions for η and γ . Therefore, we accept η and γ combinations that are within 2° of the above minimum average score. The possible η and γ combinations are therefore $(64^\circ, 39^\circ)$, $(64^\circ, 40^\circ)$, $(65^\circ, 37^\circ)$, $(65^\circ, 38^\circ)$, $(65^\circ, 39^\circ)$, $(65^\circ, 40^\circ)$, $(66^\circ, 38^\circ)$, $(66^\circ, 39^\circ)$, and $(67^\circ, 38^\circ)$.

These results show that a cone with an elliptical base describes the LUKÉ observations best. The cone is rather elongated, given both orthogonal half-angles. Using the 3D visualization software Blender, which can be used for the simulation of solar system objects (Penttilä et al. 2022), we simulated the solution including solar illumination. These simulations are shown in Figure 8. It can be seen from this figure that the simulations closely reproduce the LUKÉ observations for IDs 2 through 7. However, the simulations for IDs 1 and 8 seem to be somewhat different from the corresponding real LUKÉ images. We also note that the

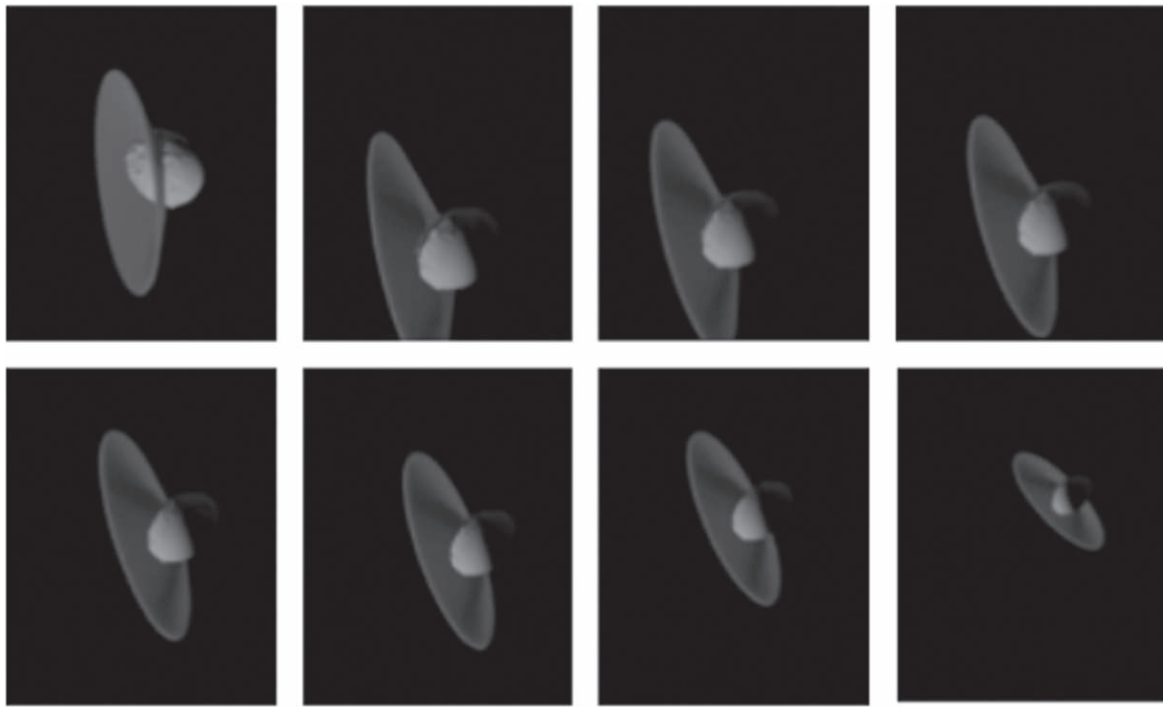


Figure 8. Simulations of LUKE observation IDs 1-8 using the axis solution of R.A., decl.: $136^\circ, +5^\circ$ using a cone with an elliptical base defined by $\eta = 64^\circ, \gamma = 39^\circ$. The top panel corresponds to IDs 1 through 4, and the bottom panel corresponds to IDs 5 through 8.

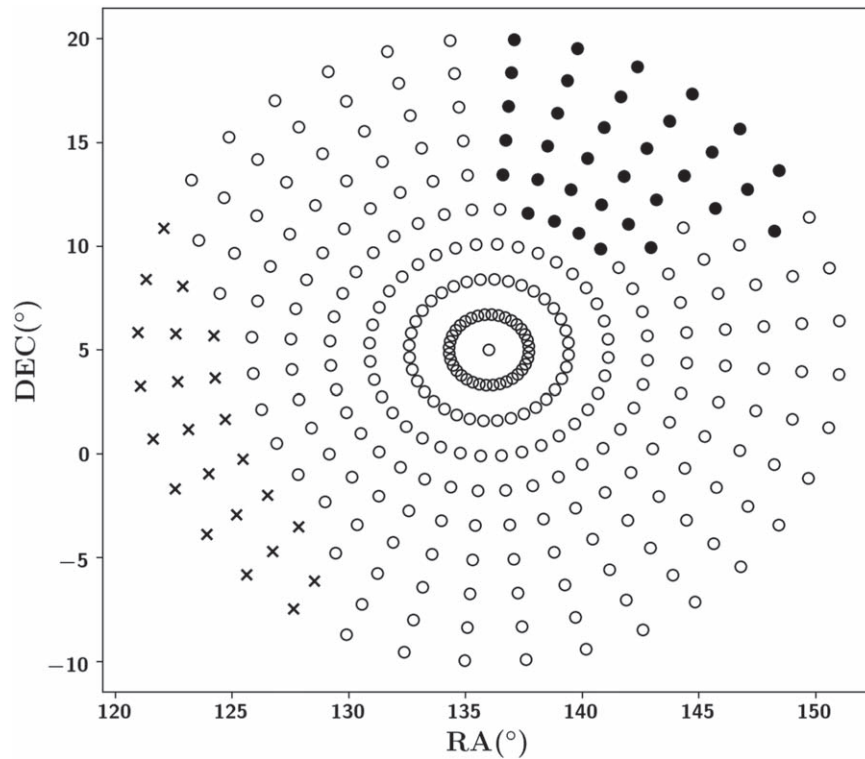


Figure 9. The sampling of the cone axes in the 15° radius uncertainty region around R.A., decl.: $136^\circ, +5^\circ$. For each axis, we have computed the best solution that fits LUKE observation IDs 2-7. Each axis therefore has a combination of R.A., decl., η , γ , and ω that defines their best score in fitting the data. The lower the score, the better the reproduction of LUKE observations. Axes with best scores lower than 6° are represented as circles, whereas axes with best scores greater than 6° are represented as crosses. The filled circles correspond to axes with solutions that are compatible with the observation ID 1, while empty circles correspond to solutions that do not agree with the observation ID 1. The solutions corresponding to the filled circles are listed in Table A1.

simulations do not reproduce the shadow of the optically thick part of the ejecta cone cast onto the surface of Dimorphos, which is evident as a dark arc on Dimorphos in

real LUKE images. Although IDs 1 and 8 serve as visual tiebreakers for the solutions we obtain, we are unable to quantify the information of the ejecta cone in these two

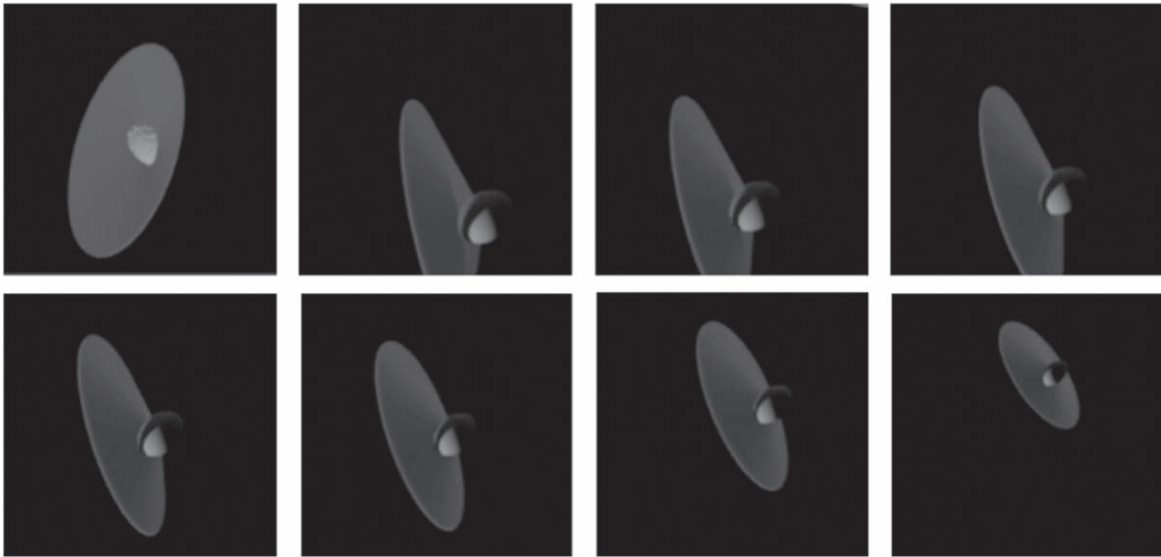


Figure 10. Simulations of LUKE observation IDs 1-8 using the axis solution of R.A., decl.: $147^\circ, +16^\circ$ using a cone with an elliptical base defined by $\eta = 69^\circ$, $\gamma = 51^\circ$, and $\omega = 12^\circ$. The top panel corresponds to IDs 1 through 4, and the bottom panel corresponds to IDs 5 through 8.

images (because ID 1 shows a face-on view of the cone, and ID 8 corresponds to a geometry close to from directly behind the cone) to further constrain the solutions. Therefore, to better reproduce the real LUKE images, we next attempt to model the observations including rotation to the cone with an elliptical base around the cone axis.

2.3. A Rotated Cone with An Elliptical Base

We introduce a rotation to the local X - and Y -axes for the cones with an elliptical base around their Z -axis, so that different geometries that were not captured in our previous methods are included in this model. At the same time, we consider an uncertainty of 15° in all directions for our current solution of the cone axis. We note that as for the current nonrotated axis solution of R.A., decl.: $136^\circ, +5^\circ$, the X - and Y -axes of the apex-centered cone coordinate system point to R.A., decl.: $33^\circ, +69^\circ$ and R.A., decl.: $228^\circ, +20^\circ$, respectively. Then, we angularly sample the region in space defined by a radius of 15° centered around the current axis solution. Following our sampling, this step leads to 324 axis vectors. For a given axis vector in this region, we seek to find cones with an elliptical base that best fit LUKE observation IDs 2-7. Each cone is systematically rotated around its axis at each iteration with five-degree increments until each cone completes a 360° rotation. This process gives us a list of cone axes with best scores corresponding to rotated cones (Figure 9). Hereafter, ω is used to refer to the angle of rotation of the X - and Y -axes around the Z -axis of the cones. As can be seen from Figure 9, a plethora of axes is combined with suitable rotated cones that match observation IDs 2-7. In order to filter the results, we first impose a threshold score of 6° , and this results in 302 cone axes that contain better (lower) scores than 6° for their solutions composed of cones with an elliptical base with rotations. Second, we imposed a constraint using the unique geometry of the observation ID 1, where the ejecta cone is observed in a face-on profile. To achieve this, we simulated this observation for all the current solutions and screened out solutions that did not match. This led to 34 solutions that now are compatible with observation IDs 1-7, and each solution is

described by a unique combination of R.A., decl., η , γ , and ω , as listed in Table A1. Each of these solutions can therefore reproduce LUKE observation IDs 1-7 at different accuracies.

To find the best possible solution, we proceeded by qualitatively analyzing the simulations of observation IDs 1-8 for each solution. By comparing the simulations with real data, it is possible to note that some solutions reproduce the dark arc on Dimorphos at different accuracies, which are present due to the shadows cast by the optically thick parts of the ejecta cone. This led us to the solution ID 24, defined by R.A., decl.: $147^\circ, +16^\circ$, $\eta = 69^\circ$, $\gamma = 51^\circ$, and $\omega = 25^\circ$ as the best solution. However, we found that a $\omega = 12^\circ$ would make this solution a better match for observation ID 8, while not affecting the other observation IDs significantly. This solution is illustrated in Figure 10.

Following this analysis, we place uncertainties depending on the distributions of R.A., decl., η , and γ on the final 34 solutions. The axis solution therefore becomes R.A., decl.: $147_{-10}^{+10}, +16_{-6}^{+4}$. The geometry of the cone with an elliptical base is described by $\eta = 69_{-30}^{+10}$, $\gamma = 51_{-11}^{+10}$. It does not make sense to place a general uncertainty for ω as the required rotation to fit the data is highly sensitive to the combinations of various variables that compose the solution itself. This can further be noted from the distributions of ω listed in Table A1. We further note that the cone axis makes an angle of 18.6° with the incoming direction of the DART spacecraft and an angle of 6.3° with the normal vector at the impact site. We remark that these findings are consistent with those reported for the ejecta cone by Hirabayashi et al. (2023) within the given uncertainties.

2.4. The Location of the Cone Apex

The derivation of the location of the cone apex is independent from the solution of the ejecta cone. To achieve this, we make use of the side-on views of the ejecta cone observed in image IDs 2 to 6. The edges that are highlighted in Figure 2 allow us to define the projected apex of the cone in the LUKE image plane. Hence, for each considered image, we can find the boresight of the pixel that goes through the projected

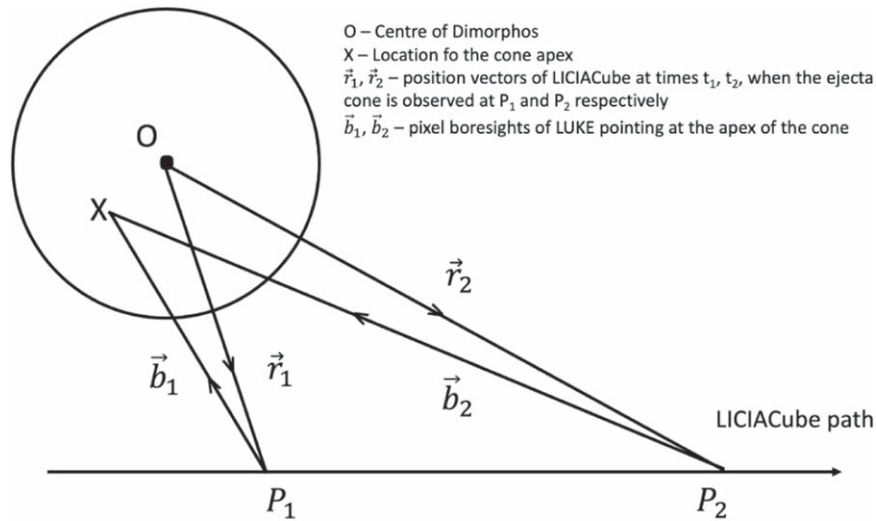


Figure 11. Geometry of LICIACube observations that were used to derive the location of the cone apex.

apex of the cone. We assume that the boresight of the corresponding pixel goes through the apex of the cone. If we consider two observations, we can define a plane in three-dimensional inertial space, using the locations of LICIACube at the two observations and the location of the apex (Figure 11). Thus, knowing the location of the LICIACube at the given two instances and the boresight vectors of the projected apices, we can develop parametric vector equations to solve for the location of the apex. Then, we transform this location to the body-fixed coordinate system of Dimorphos (IAU-DIMORPHOS). In our solution, we used IDs 2 and 6 (combination with the largest baseline) to solve for the apex, and other observations were used to place the uncertainties. Based on this, we report the location of the cone apex to be -11_{-4}^{+18} , 9_{-20}^{+10} , -4_{-14}^{+18} m in the Dimorphos coordinate system. The apex is thus located at about 15 m from the center of Dimorphos. The solution of the cone apex is also consistent with the apex location derived (using a different assumption and method) by Hirabayashi et al. (2023) within the uncertainties.

3. Discussion

We modeled the ejecta plume triggered by the DART impact on Dimorphos starting with a simple cone model with a circular base, and we developed it into a more complicated rotated cone with an elliptical base. It is noteworthy that our axis solution of R.A., decl.: 147_{-10}^{+10} , $+16_{-6}^{+4}$ is slightly different from the cone axis solution of Dotto et al. (2023), who report an axis solution of R.A., decl.: 137_{-9}^{+8} , $+19_{-12}^{+10}$. This discrepancy is due to the nature of the SPICE kernels that were used at different stages of the LICIACube mission. The solution of Dotto et al. (2023) was derived from a set of SPICE kernels available in 2022 December, whereas our solution corresponds to the latest LICIACube SPICE kernels available at the writing of this work (2023 September). The previous kernels had a twist-angle uncertainty of about 15° at the time of closest approach with the Didymos system, which were later corrected, leading to the latest iteration of the kernels that we used in this work.

Some works that modeled the ejecta cone have assumed (Cheng et al. 2023; Li et al. 2023) that the cone axis lies in the bisector of the projected images of the ejecta cone in the observed images. However, the axis of a cone with an elliptical base does not necessarily lie in the bisector of its projection.

Although we started our modeling with a similar assumption in Section 2.1, we allowed the cone axis to vary in an uncertainty region in Section 2.3 with free rotation. We therefore considered and explored potential solutions that are not captured in the methods used by these works. This explains the difference of the results in this work and the aforementioned works, although the results from different authors agree among themselves within the given uncertainties. We refer to the work by Hirabayashi et al. (2023), who use both LICIACube and HST data to find solutions to the geometry and the orientation of the ejecta cone using statistical methods. We note that our results confirm theirs and are consistent within the uncertainties for the half-angles, the direction, and the apex of the ejecta cone. These independent methods arriving at the same result provide validation and enhance the confidence in the accuracy and reliability of the findings.

In our methods, we also remark that we have assumed that the ejecta plume remained fixed during its observations by LUKE. However, there is a time span of about 30 seconds between image ID 1 and ID 8 that went into this analysis. During this time span, the physical features that compose the ejecta plume were expanding at projected velocities up to 75 m s^{-1} (Dotto et al. 2023). The ejecta plume showed a complex dynamical structure that cannot be trivially described by a geometrical structure, even with a more elaborated approximation of a cone with an elliptical base, which is what we have attempted in this work. Nevertheless, as seen in Figure 10, we reproduce LUKE observation IDs 1 through 8 with high accuracy, following an approach that combined both quantitative and qualitative analyses. Notably, we reproduce the dark arc present on Dimorphos in our Blender-based simulations. We stress that it would require precise dust dynamical and radiative-transfer modeling if one were to reproduce LUKE observations with high fidelity. The fact that we lack information about the physical properties of the Dimorphos material, their size-frequency distributions, and so on makes it furthermore a task that is hard to achieve. Nevertheless, given that the LUKE images contain the flux of the ejecta plume and that we have now established the three-dimensional structure and the orientation of the ejecta plume, this will allow us by means of radiative-transfer simulations (P.

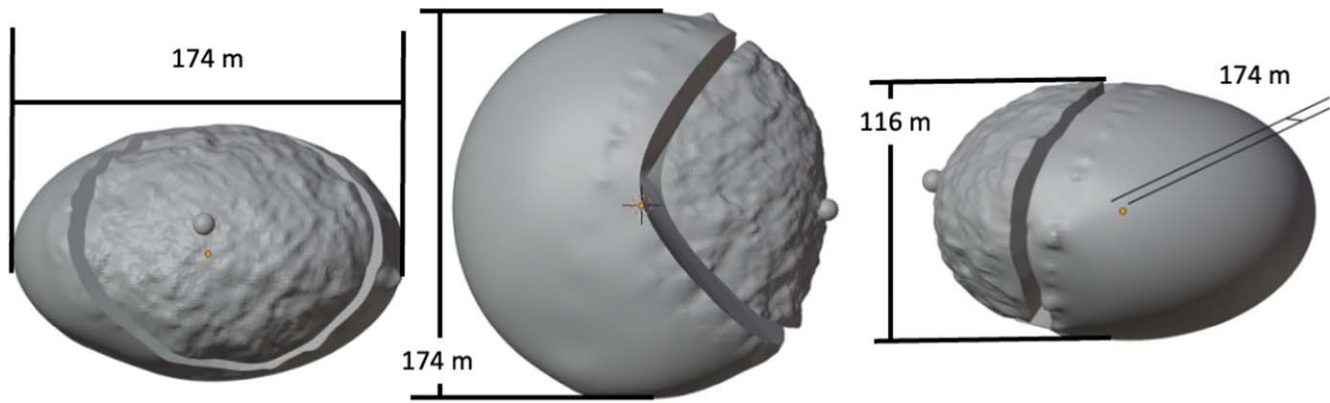


Figure 12. Three orthogonal views of the intersection of the ejecta cone and the surface of the Dimorphos, leading to the definition of the perimeter of the crater created by the DART impact. The sphere with a radius of 10 m shows the location of the DART impact. The orange dot marks the center of Dimorphos.

Table 2
Summary of the Main Results in This Work

Quantity	Symbol	Value	Unit	Comments
Cone axis R.A.	RA	147_{-10}^{+1}	degrees	in J2000
Cone axis decl.	DEC	$+16_{-6}^{+4}$	degrees	in J2000
Cone wide half-angle	η	69_{-3}^{+1}	degrees	...
Cone narrow half-angle	γ	51_{-11}^{+1}	degrees	...
Cone XY axes rotation angle	ω	12	degrees	...
Angle between the cone axis and the DART incoming direction	...	18.6	degrees	...
Angle between the cone axis and the impact surface normal	...	6.3	degrees	...
Cone apex (x,y,z)	...	$-11_{-4}^{+18}, 9_{-20}^{+10}, -4_{-14}^{+18}$	m	in IAU-DIMORPHOS
Crater equivalent radius	...	65	m	...

H. Hasselmann et al. 2023, in preparation) to place constraints on the physical properties of the plume particles, assuming that the two binary components share the same composition (Margot et al. 2015). The physical properties can be further constrained through dust dynamical simulations of different shapes of ejected clumps of material observed in the ejecta cone (S. Ivanovski et al. 2023, in preparation).

We note that the apex of the ejecta cone is located close to the center of Dimorphos (within 15 m), in contrast to the estimates and simulations of LICIACube observations implemented prior to the impact event (Fahnestock et al. 2022; Kolokolova et al. 2022). The fact that the apex is located much closer to the center than the surface implies that the crater generated by the impact may have been in a gravity-dominated regime as opposed to a strength-dominated regime, which could be preferred prior to the impact owing to an S-type taxonomic composition linked with L/LL meteorites. This observation is supported by the work of Raducan et al. (2023), who point out the likelihood that Dimorphos underwent reshaping following the impact because it was not within a regime dominated by strength. It is interesting to note that the impact crater produced on asteroid Ryugu by the Small Carry-on Impactor (SCI) as part of the JAXA Hayabusa2 mission (Watanabe et al. 2017) was in a gravity-dominated regime as opposed to a strength-dominated regime, which was contrary to the predictions (Arakawa et al. 2017, 2020). Indeed, the crater created by the SCI corresponded to a diameter of 15 m, whereas the predictions had implied a diameter of a few meters only. Furthermore, we confirm that a shadow is cast on Dimorphos by the optically thick part of the ejecta cone, as predicted by Cheng et al. (2022). Our simulations closely

reproduce this shadow, with the apex of the cone being placed close to the center of Dimorphos. Our simulations show that if the apex were to be placed closer to the surface of Dimorphos, the shadows would be much different from what was observed by LUKE. We computed the intersection of the ejecta cone and the surface of Dimorphos and projected the intersection to a plane that is perpendicular to the cone axis. This projected perimeter was about 407 m. While this estimation is purely geometrical, if the projected cone-surface intersection is a direct interpretation of the crater size, the measured cone geometry suggests an equivalent crater radius of 65 m (Figure 12). We note that Hirabayashi et al. (2023) give the average distance between the impact point and the surface-cone intersection as 76 m. However, this difference is reasonable because the impact point is not on the plane defined by the perimeter, and hence, the determined radius in our work should be shorter than the distance measured by Hirabayashi et al. (2023). Therefore, this value may be used as an upper limit, and we highlight that more sophisticated physical models should be used for more realistic estimates (Raducan et al. 2023; Stickle et al. 2023). Nevertheless, this value exceeds the estimated crater radii for different impact scenarios by studies conducted prior to the impact event (radii in the range of 5–45 m in Cheng et al. 2022 and in the range of 13–21 m in Fahnestock et al. 2022). The ground truth of this crater will be revealed as its morphology will be mapped by the ESA Hera mission, which will visit and rendezvous with the Didymos system in 2026 December (Michel et al. 2018, 2022). The observations by Hera will thus confirm whether the impact was in a strength-dominated or a gravity-dominated regime.

4. Conclusions

Following our modeling of the DART-induced ejecta plume on Dimorphos, we conclude that the geometry of the ejecta plume can be best approximated by a cone with an elliptical base, despite some intricacies such as extended structures composing both clumps of material and individual grains in expansion, which are observed in LUKE data, but are not fully captured in our model. Table 2 recapitulates the main results of this work. The elliptical nature of the cone, characterized by a combination of a wide half-angle (69°) and a narrow half-angle (51°), can be due to several factors, such as the curvature of the impact surface (Schultz et al. 1987; Hirabayashi et al. 2023; P. Sanchez et al. 2023, in preparation), the geometry of the impactor (the DART spacecraft, including its solar panels; Raducan et al. 2022), and the presence or absence of boulders on the impact location. The computed relatively large upper limit of the radius of the resulting crater implies that the impact may have been in a gravity-dominated regime rather than a strength-dominated one. In situ observations of impacts like this and that of SCI by Hayabusa2 could potentially reveal more insights about the impact physics and ejecta scaling laws and place constraints on the material properties of the asteroids (Housen & Holsapple 2011). They could equally be important in terms of planetary defence scenarios by means of kinetic impactors to accurately estimate β , depending on whether the impact takes place in a strength-dominated or a gravity-dominated regime.

The results of this work also highlight the prowess of CubeSat solutions for bootstrapping planetary missions to maximize the scientific return, as has been shown by LICIAcube.

Acknowledgments

J.D.P.D. thanks the friendly folks of the Hiking Crew in Rome for their kind support in numerous ways. The LICIAcube team acknowledges financial support from Agenzia Spaziale Italiana (ASI, contract No. 2019-31-HH.0 CUP F84I190012600). This work was supported by the DART mission, NASA Contract 80MSFC20D0004. Work by E.G.F. was carried out at the Jet Propulsion Laboratory, California Institute of Technology, under a contract with the National Aeronautics and Space Administration (#80NM0018D0004).

Software: python, astropy (Astropy-Collaboration et al. 2013), SAOImageDS9 (Joye & Mandel 2003), Blender, pyvista (Sullivan & Kaszynski 2019), numpy (van der Walt et al. 2011), pandas (Wes McKinney 2010), matplotlib (Hunter 2007), spiceypy (Annex et al. 2020), pyquaternion, Microsoft PowerPoint, texmaker, JabRef, Atom.

Appendix

Potential Axis Solutions Including Rotations














Table A1 lists the potential solutions that correspond to the best scores for the considered observations.

Table A1
The 34 Solutions That Best Describe LUKE Observation IDs 1-7 of the Ejecta Cone

ID	R.A. ($^\circ$)	Decl. ($^\circ$)	Best Score ($^\circ$)	η ($^\circ$)	γ ($^\circ$)	ω ($^\circ$)
1	139	15	3.34	68	41	35
2	142	13	3.39	68	45	25
3	137	17	3.39	68	40	40
4	137	15	3.48	68	40	35
5	138	13	3.49	67	42	25
6	139	11	3.52	67	41	25
7	139	16	3.54	68	44	30
8	141	16	3.56	68	45	30
9	142	19	3.57	69	47	35
10	147	13	3.59	69	49	25
11	137	13	3.60	67	40	30
12	146	15	3.60	69	49	25
13	145	17	3.67	70	49	30
14	148	14	3.68	69	52	20
15	142	17	3.70	70	45	35
16	144	13	3.71	69	47	25
17	140	14	3.75	68	43	30
18	148	11	3.77	69	51	15
19	139	18	3.78	69	43	40
20	137	20	3.84	70	41	45
21	141	10	3.88	66	43	20
22	143	15	3.95	68	47	25
23	140	20	4.00	70	44	40
24	147	16	4.04	69	51	25
25	144	16	4.08	70	47	30
26	141	12	4.09	68	43	25
27	140	13	4.15	67	43	25
28	137	18	4.16	68	42	40
29	143	12	4.20	69	45	25
30	138	12	4.34	67	40	25
31	142	11	4.41	67	45	20
32	146	12	4.49	69	48	20
33	140	11	4.51	66	45	10
34	143	10	4.60	66	46	15

Note. The solutions are listed in descending order with respect to the best score. Each solution is a combination of an axis defined by R.A., decl. in the J2000 inertial frame, a cone with an elliptical base that is defined by η and γ , and a rotation of ω around the local Z-axis of the cone.

ORCID iDs

J. D. P. Deshapriya  <https://orcid.org/0000-0002-5758-1286>
P. H. Hasselmann  <https://orcid.org/0000-0003-1193-8945>
M. Hirabayashi  <https://orcid.org/0000-0002-1821-5689>
A. Rossi  <https://orcid.org/0000-0001-9311-2869>
A. Zinzi  <https://orcid.org/0000-0001-5263-5348>
S. Ieva  <https://orcid.org/0000-0001-8694-9038>
M. Dall’Ora  <https://orcid.org/0000-0001-8209-0449>
S. Ivanovski  <https://orcid.org/0000-0002-8068-7695>
D. Perna  <https://orcid.org/0000-0002-4545-3850>
T. L. Farnham  <https://orcid.org/0000-0002-4767-9861>
J. R. Brucato  <https://orcid.org/0000-0002-4738-5521>
Nancy L. Chabot  <https://orcid.org/0000-0001-8628-3176>
G. Cremonese  <https://orcid.org/0000-0001-9021-1140>

R. T. Daly [ORCID](https://orcid.org/0000-0002-1320-2985) <https://orcid.org/0000-0002-1320-2985>
 M. Pajola [ORCID](https://orcid.org/0000-0002-3144-1277) <https://orcid.org/0000-0002-3144-1277>
 E. Palmer [ORCID](https://orcid.org/0000-0001-6755-8736) <https://orcid.org/0000-0001-6755-8736>
 P. Palumbo [ORCID](https://orcid.org/0000-0003-2323-9228) <https://orcid.org/0000-0003-2323-9228>
 G. Poggiali [ORCID](https://orcid.org/0000-0002-3239-1697) <https://orcid.org/0000-0002-3239-1697>
 A. S. Rivkin [ORCID](https://orcid.org/0000-0002-9939-9976) <https://orcid.org/0000-0002-9939-9976>
 P. Sanchez [ORCID](https://orcid.org/0000-0003-3610-5480) <https://orcid.org/0000-0003-3610-5480>
 G. Tancredi [ORCID](https://orcid.org/0000-0002-4943-8623) <https://orcid.org/0000-0002-4943-8623>

References

- Acton, C., Bachman, N., Semenov, B., & Wright, E. 2018, *P&SS*, **150**, 9
 Acton, C. H. 1996, *P&SS*, **44**, 65
 Annex, A., Pearson, B., Seignovert, B., et al. 2020, *JOSS*, **5**, 2050
 Arakawa, M., Saiki, T., Wada, K., et al. 2020, *Sci*, **368**, 67
 Arakawa, M., Wada, K., Saiki, T., et al. 2017, *SSRv*, **208**, 187
 Astropy-Collaboration, Robitaille, T. P., Tollerud, E. J., et al. 2013, *A&A*, **558**, A33
 Chen, H.-S., & Stadtherr, M. A. 1981, *Comput. Chem. Eng.*, **5**, 143
 Cheng, A. F., Agrusa, H. F., Barbee, B. W., et al. 2023, *Natur*, **616**, 457
 Cheng, A. F., Raducan, S. D., Fahnestock, E. G., et al. 2022, *PSJ*, **3**, 131
 Cheng, A. F., Rivkin, A. S., Michel, P., et al. 2018, *P&SS*, **157**, 104
 Dotto, E., Della Corte, V., Amoroso, M., et al. 2021, *P&SS*, **199**, 105185
 Dotto, E., Deshapriya, J. D. P., Gai, I., et al. 2023, *Natur*, submitted
 Fahnestock, E. G., Cheng, A. F., Ivanovski, S., et al. 2022, *PSJ*, **3**, 206
 Hirabayashi, M., Raducan, S. D., Sunshine, J. M., et al. 2023, *NatCo*, submitted
 Housen, K. R., & Holsapple, K. A. 2011, *Icar*, **211**, 856
 Hunter, J. D. 2007, *CSE*, **9**, 90
 Joye, W. A., & Mandel, E. 2003, in ASP Conf. Ser. 295, *Astronomical Data Analysis Software and Systems XII*, ed. H. E. Payne, R. I. Jedrzejewski, & R. N. Hook (San Francisco, CA: ASP), 489
 Kolokolova, L., Li, J.-Y., van Selous, M., Farnham, T., & Nagdimunov, L. 2022, *PSJ*, **3**, 262
 Li, J.-Y., Hirabayashi, M., Farnham, T. L., et al. 2023, *Natur*, **616**, 452
 Margot, J. L., Pravec, P., Taylor, P., Carry, B., & Jacobson, S. 2015, in *Asteroids IV*, ed. P. Michel, F. E. DeMeo, & W. F. Bottke (Tucson, AZ: Univ. Arizona Press), 355
 Michel, P., Kueppers, M., Sierks, H., et al. 2018, *AdSpR*, **62**, 2261
 Michel, P., Küppers, M., Bagatin, A. C., et al. 2022, *PSJ*, **3**, 160
 Penttilä, A., Palos, M. F., Näsälä, A., & Kohout, T. 2022, *EPSC*, **16**, EPSC2022-788
 Raducan, S. D., & Jutzi, M. 2022, *PSJ*, **3**, 128
 Raducan, S. D., Jutzi, M., Cheng, A. F., et al. 2023, *NatAs*, submitted
 Raducan, S. D., Jutzi, M., Davison, T. M., et al. 2022, *IJIE*, **162**, 104147
 Rivkin, A. S., Chabot, N. L., Stickle, A. M., et al. 2021, *PSJ*, **2**, 173
 Schultz, P. H., Gault, D. E., & Crawford, D. 1987, *Impacts of Hemispherical Granular Targets: Implications for Global Impacts*, Reports of Planetary Geology and Geophysics Program, Murphys Center of Planetology **380**
 Stickle, A. M., DeCoster, M. E., Burger, C., et al. 2022, *PSJ*, **3**, 248
 Stickle, A. M., Kumamoto, K. M., DeCoster, M. E., et al. 2023, *NatGeo*, submitted
 Sullivan, C., & Kaszynski, A. 2019, *JOSS*, **4**, 1450
 Thomas, C. A., Naidu, S. P., Scheirich, P., et al. 2023, *Natur*, **616**, 448
 van der Walt, S., Colbert, S. C., & Varoquaux, G. 2011, *CSE*, **13**, 22
 Watanabe, S.-i., Tsuda, Y., Yoshikawa, M., et al. 2017, *SSRv*, **208**, 3
 Wes McKinney 2010, in Proc. of the 9th Python in Science Conf., ed. Stéfan van der Walt & Jarrod Millman, 56